RESEARCH ARTICLE

Fuel Cells

Energy & Environmental Materials WILEY

Reducing Critical Raw Material Use in Commercial Solid Oxide Fuel Cells Using Vertically Aligned Thin-Film Cathodes with Enhanced Long-Term Stability

Matthew P. Wells, Kosova Kreka, Mohana V. Kante, Miriam Botros, Ozden Celikbilek, Jan Pieter Ouweltjes, Federico Baiutti, Simon M. Fairclough, Caterina Ducati, Albert Tarancón, and Judith L. MacManus-Driscoll*

Solid oxide fuel cells (SOFCs) are widely presented as a sustainable solution to future energy challenges. Nevertheless, solid oxide fuel cells presently rely on significant use of several critical raw materials to enable optimized electrode reaction kinetics. This challenge can be addressed by using thin-film electrode materials; however, this is typically accompanied by complex device fabrication procedures as well as poor mechanical/chemical stability. In this work, we conduct a systematic study of a range of promising thin-film electrode materials based on vertically aligned nanocomposite (VAN) thin films. We demonstrate low area specific resistance (ASR) values of 0.44 cm^2 at 650 °C can be achieved using $(La_{0.60}Sr_{0.40})_{0.95}Co_{0.20}Fe_{0.80}O_3$-$(Sm_2O_3)_{0.20}(CeO_2)_{0.80}$ (LSCF-SDC) thin films, which are also characterized by a low degradation rate, approximately half that of planar LSCF thin films. We then integrate these $(La_{0.60}Sr_{0.40})_{0.95}Co_{0.20}Fe_{0.80}O_3$-$(Sm_2O_3)_{0.20}(CeO_2)_{0.80}$ vertically aligned nanocomposite films directly with commercial anode supported half cells through a single-step deposition process. The resulting cells exhibit peak power density of 0.47 W cm^{-2} at 750 °C, competitive with 0.64 W cm^{-2} achieved for the same cells operating with a bulk $(La_{0.60}Sr_{0.40})_{0.95}Co_{0.20}Fe_{0.80}O_3$ cathode, despite 99.5% reduction in cathode critical raw material use. By demonstrating such competitive performance using thin-film cathode functional layers, this work also paves the way for further cost reductions in solid oxide fuel cells, which could be achieved by likewise applying thin-film architectures to the anode functional layer and/or current collecting layers, which typically account for the greatest materials cost in solid oxide fuel cell stacks. Therefore, the present work marks a valuable step towards the sustainable proliferation of solid oxide fuel cells.

1. Introduction

Solid oxide fuel cells (SOFCs) have regularly been proposed as a promising solution for future portable power applications due to their efficient conversion between chemical and electrical energy.[1–5] To overcome sluggish electrode reaction kinetics, SOFCs presently rely on the use of several rare-earth elements and other critical raw materials (CRMs) such as Co, La, Ce, Gd, Sr, Y, Pr, Pt, and Ni.[6] This comes at significant economic and ecological cost, and is prohibitive to the sustainable proliferation of SOFC technology.[1,6] In this work, we overcome this challenge through the use of vertically aligned nanocomposite thin-film cathodes, which we show can be directly integrated with commercial SOFC devices to replace conventional bulk cathodes.

Thin-film electrodes (<500 nm thickness) offer a direct means to significantly reduce CRM loading in practical devices. Although bulk materials have typically outperformed their thin-film counterparts, recent years have seen significant advances in the design of thin-film SOFC electrodes through the introduction of new materials classes such as vertically aligned nanocomposite (VAN) films and high entropy oxides (HEOs), both of which have been noted for their exceptional long-term stability characteristics, in addition to strategies such as oxygen

Dr M. P. Wells, Dr S. M. Fairclough, Prof C. Ducati, Prof J. L. MacManus-Driscoll
Department of Materials Science and Metallurgy, University of Cambridge, 27 Charles Babbage Road, Cambridge CB3 0FS, UK
E-mail: mpw52@cam.ac.uk
Dr. K. Kreka, Dr F. Baiutti, Prof A. Tarancón
Department of Advanced Materials for Energy, Catalonia Institute for Energy Research (IREC), 1 Jardins de les Dones de Negre, Barcelona 08930, Spain
M. V. Kante, Dr M. Botros
Institute of Nanotechnology, Karlsruhe Institute of Technology (KIT), Hermann-von-Helmholtz Platz 1, 76344, Eggenstein-Leopoldshafen, Germany
Dr O. Celikbilek
Department of Materials, Imperial College London, Exhibition Road, London SW7 2AZ, UK
J. P. Ouweltjes
SolydEra SpA, Viale Trento 117, Mezzolombardo, Italy
Prof A. Tarancón
ICREA, Passeig Lluís Companys 23, Barcelona 08010, Spain
The ORCID identification number(s) for the author(s) of this article can be found under https://doi.org/10.1002/eem2.70011.

DOI: 10.1002/eem2.70011

defect engineering and thin-film surface modifications to optimize reaction kinetics.[7–14] To date, however, the commercialization of these advances in thin-film-based SOFCs has been prohibited by complex fabrication procedures and/or fragile device structures.[11,15,16] Future widespread use of SOFCs therefore demands the successful integration of thin-film electrodes with commercial fabrication procedures.

Recent work by Machado et al.[17] has revealed the advantages of nanocomposite thin films acting as interlayers in commercial anode supported SOFCs with bulk $(La_{0.6}Sr_{0.4})_{0.95}Co_{0.2}Fe_{0.8}O_3$ (LSCF) cathodes. Here, the addition of a 200-nm-thick $La_{0.8}Sr_{0.2}MnO_3$-$Ce_{0.8}Sm_{0.2}O_2$ (LSM-SDC) nanocomposite interlayer between the electrolyte and LSCF cathode, both of bulk form, increased peak power density from 0.64 to 1.00 W cm^{-2} at 750 °C. This demonstrates that state-of-the-art nanocomposite thin films can be integrated with commercial cells; however, despite recent efforts on removing bulk materials from the electrodes,[18] the challenge of reducing CRMs by using thin films remains pertinent. This challenge demands a broad survey of candidate thin-film electrode materials, especially regarding the long-term stability of the nanomaterials employed.

In this work, we show that bulk SOFC cathodes can indeed be replaced by thin films in commercial SOFC devices. Firstly, we study a range of promising candidate thin-film cathode materials deposited by pulsed laser deposition (PLD) on polycrystalline $(Y_2O_3)_{0.08}(ZrO_2)_{0.92}$ (YSZ) substrates. We show that LSCF-SDC nanocomposite films exhibit ASR values of 0.44 cm^2 at 650 °C, representing a 46% reduction compared with planar LSCF films together with improved long-term stability characteristics. We then directly integrate the LSCF-SDC thin-film cathode into commercial anode supported half cells, entirely replacing the typical bulk LSCF cathode with a single-step PLD process. The optimized processing steps allow for the incorporation of compositionally complex materials, for example, high entropy oxides (HEOs), offering a further route to reducing CRMs. Cells with only the LSCF-SDC thin-film cathode deliver peak power output of 0.47 W cm^{-2} at 750 °C compared to 0.64 W cm^{-2} achieved with commercial bulk LSCF, despite a 99.5% reduction in LSCF content. We also demonstrate reversible operation of the cells, achieving 0.4 A cm^{-2} at 1.4 V in electrolysis mode at 700 °C. Therefore, the present work demonstrates that thin-film SOC electrodes can be successfully combined with simple fabrication procedures to achieve drastic reduction in SOC critical raw material use and thus enable commercial viability of SOC devices.

2. Results

A range of seven candidate cathode thin films are studied herein. Planar LSCF thin films were selected to provide a benchmark with conventional cathode materials.[19,20] VAN film compositions were selected based on exceptional performance demonstrated in previous works, including LSCF-SDC,[16] Ag-$Gd_{0.20}(CeO_2)_{0.80}$ (Ag-CGO),[21] and etched LSCF-MgO films (in which the MgO phase of the nanocomposite structure is selectively etched to leave a high surface area mesoporous LSCF network).[9,11] Additionally, we explore a novel high entropy oxide with composition $(Ce_{0.2}La_{0.2}Sm_{0.2}Pr_{0.2}Y_{0.2})O_2$; such HEOs have been shown to offer promising electrochemical performance and exceptional high temperature stability over long-term operation.[14] Furthermore, we introduce for the first time a HEO-based VAN cathode, with the aim of overcoming the oxygen diffusion-limited performance of the planar HEO as discussed later.

The seven candidate planar (LSCF and HEO) and VAN (Ag-CGO, LSCF-SDC, LSCF-MgO, and LSCF-HEO) films were deposited on SDC-buffered polycrystalline YSZ tape as well as single-crystal YSZ substrates and X-ray diffraction (XRD) measurements (Figure S1, Supporting Information) confirm deposition of the desired material phases. Epitaxial growth is observed in planar and VAN films deposited on single-crystal substrates (Figure S1a, Supporting Information). Planar films of LSCF and HEO exhibit highly oriented/epitaxial growth in the expected (hk0) and (h00) directions, respectively. In the LSCF-SDC and LSCF-HEO films, both phases have similar lattice parameters (accounting for a 45° rotation in LSCF) and so both are able to grow epitaxially, consistent with previous literature on VAN films.[16,22] For LSCF-SDC films, there is significant overlap between the LSCF (110) and SDC (200) peaks; therefore, a Reciprocal Space Map (RSM) around the YSZ (−205) peak is shown in Figure S2, Supporting Information, from which the SDC (−205) and LSCF (−114) peaks are observed, thus demonstrating clear distinction between the two phases. Meanwhile, the VAN films containing MgO and Ag show highly oriented/epitaxial growth of one phase (i.e., (hkl) oriented MgO; (h00) oriented CGO), with multiple orientations of the other phase (i.e., (h00), (hk0), and (hkl) oriented LSCF), owing to the large structural differences between MgO/Ag and LSCF/GDC, respectively.

For the same films grown on polycrystalline YSZ tapes, the peaks corresponding to LSCF, SDC, and HEO cannot be readily distinguished from those of the SDC-buffered YSZ substrate (Figure S1b, Supporting Information). However, (111) texture is observed for Ag and MgO in Ag-CGO and LSCF-MgO nanocomposite films, respectively (Figure S1b, Supporting Information), consistent with fast close packed growth directions in these cubic structures.

Electrochemical impedance spectroscopy (EIS) was performed on symmetric samples grown on polycrystalline YSZ tapes, and the area specific polarization resistance (ASR_p) values for each material are presented in **Figure 1a**, together with representative Nyquist plots in Figure 1b. Figure 1a also provides comparison to the ASR_p values of gold paste, and to bulk LSCF with a thin-film LSM-SDC nanocomposite interlayer (LSM-SDC + LSCF) as reported by Machado et al.[17] The high impedance of the gold paste confirms that the Au acts solely as a current collector and has a negligible impact on the measured impedance of the other candidate cathode materials. By contrast, LSM-SDC + LSCF represents a high performance benchmark, with $ASR_p = 0.4\ \Omega cm^2$ at 600 °C.

We note here recent works by Develos-Bagarinao et al.,[23] who report that LSCF-CGO nanocomposite films used together with bulk $La_{0.6}Sr_{0.4}CoO_{3-\delta}$ (LSC) deliver lower ASR values ($\sim 0.04\ \Omega cm^2$ at 600 °C). In Figure 1 the results of the present work are given in comparison with LSM-SDC + LSCF, as these results were acquired using the same measurement setup and YSZ substrates, in addition to the same anode supported half cells, studied later. Thus, the results of the LSM-SDC + LSCF system reported by Machado et al. represent the most relevant benchmark to the present work.

The impedance responses of each cathode material were fitted to a minimum of two ZARC elements (such that the electrode response of each side of the symmetric cell is modeled by a resistor and constant phase element connected in parallel, shown schematically in Figure S3, Supporting Information). In all cases, the impedance arc corresponding to the polarization resistance of the cathode was found to have a characteristic capacitance on the order of 1×10^{-4} to 1×10^{-3} F cm^{-2} and the ASR_p was thus calculated according to Equation (1) below:

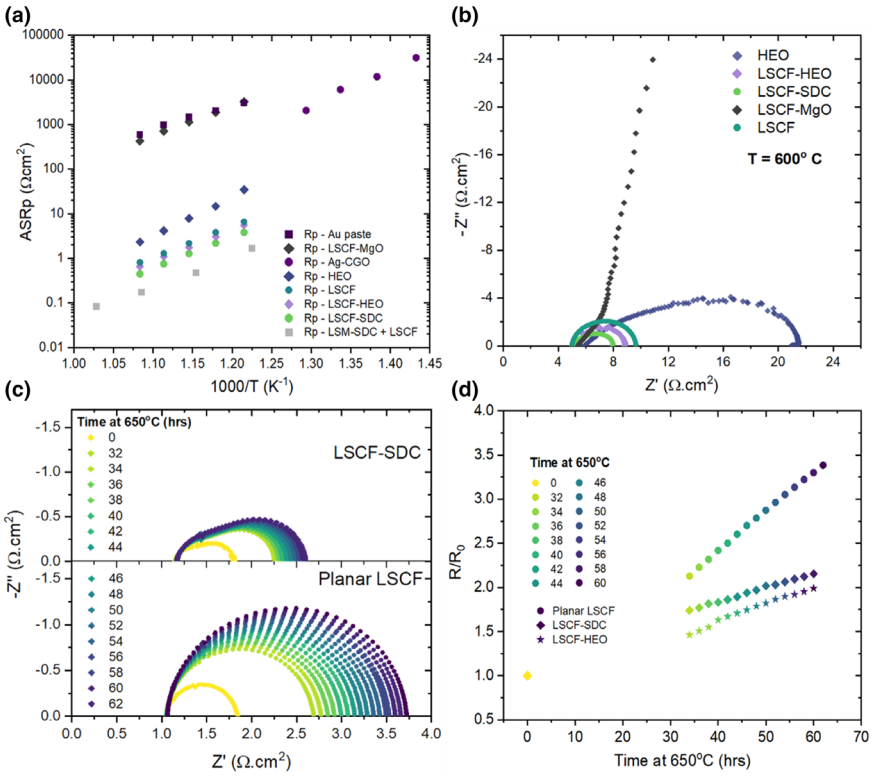

Figure 1. a) Comparison of ASRp values for symmetric cells of all thin-film materials under study grown on polycrystalline YSZ, together with benchmark values for Au paste and literature values for LSM-SDC thin films with bulk LSCF[17]; b) Nyquist plots of HEO, LSCF-HEO, LSCF-SDC, LSCF-MgO, and LSCF; c) evolution of Nyquist plots for LSCF and LSCF-SDC films showing reduced degradation in LSCF-SDC nanocomposite structure; d) evolution of ASRp for LSCF, LSCF-SDC, and LSCF-HEO films held at 650 °C for 62 h.

$$\mathrm{ASR_p} = \mathrm{Area} \times \left(\frac{R_1 + R_2}{2}\right) \quad (1)$$

The fitting parameters for all samples are given in Table S1, Supporting Information, and a summary of results for all the cathode compositions under study is given in **Table 1** below. We note here that some of the materials under study (HEO, Ag-CGO, LSCF-HEO) exhibit additional features in the Nyquist plots at temperatures below 600 °C (shown in Figure S3, Supporting Information). These are modeled by an additional ZARC component with characteristic capacitance on the order 1×10^{-8} to 1×10^{-6} F cm^{-2} and are therefore ascribed to interfacial impedances within the symmetric cell structure.[24] A more detailed analysis of additional high-frequency features in the Ag-CGO was not pursued in the present work due to the complexity of isolating individual components.

From Figure 1a, we observe that the LSCF-MgO exhibits an exceptionally high impedance, with negligible reduction in $\mathrm{ASR_p}$ compared with gold paste. This is attributed to the LSCF microstructure after etching of the MgO. Unlike depositions on single-crystal substrates,[9,25] the film deposited on polycrystalline YSZ exhibits a disconnected LSCF microstructure (Figure S4, Supporting Information), thus inhibiting electronic and ionic transport.

We next consider the Ag-CGO; this material system was characterized at lower operating temperatures (≲500 °C) than the other materials under study due to the known degradation of Ag at higher temperatures. Nevertheless, $\mathrm{ASR_p}$ values over 2000 Ωcm^2 at 500 °C render Ag-CGO unsuitable for the present application. Extrapolating the Ag-CGO data to higher temperatures, and assuming no significant degradation, reveals $\mathrm{ASR_p} \sim 37$ Ωcm^2 at 650 °C; the novel $(Ce_{0.2}La_{0.2}Sm_{0.2}Pr_{0.2}Y_{0.2})O_2$ HEO thus exhibits more than one order of magnitude reduction in $\mathrm{ASR_p}$ values of Ag-CGO, with $\mathrm{ASR_p} = 2.3$ Ωcm^2 at 650 °C. The corresponding Nyquist plot in Figure 1b comprises a ∼45° straight element in the high-frequency regime, indicative of a surface exchange and diffusion co-limited response.[10] Previous studies have identified that such co-limited processes in the case of LSM can be overcome through the use of VAN structures to incorporate fast ionic conducting pathways (SDC).[10] Here, we utilize this strategy by adding an LSCF mixed ionic electronic conducting phase to the HEO. LSCF was chosen in preference to SDC in this case on the basis that the perovskite LSCF would likely form a more distinct nanocomposite structure with the HEO, as both Sm and Ce are present in the HEO composition. The representative Nyquist plot of this highly novel LSCF-HEO nanocomposite structure (Figure 1b) now reveals a near ideal impedance arc; the LSCF-HEO cathode is thus purely surface exchange limited resulting in an $\mathrm{ASR_p}$ of 0.65 Ωcm^2 at 650 °C. The LSCF-SDC nanocomposite yields a further reduction in $\mathrm{ASR_p}$, achieving 0.44 Ωcm^2 at 650 °C and marking a 46% reduction compared with planar LSCF (0.81 Ωcm^2).

Further advantages of the nanocomposite thin-film structure are revealed by considering the long-term high temperature stability. Planar LSCF thin films are well-known to degrade over time due to segregation of Sr to the film surface.[13,26] Here, Figure 1c shows clearly the degradation suffered by LSCF: Nyquist plots are shown for LSCF films in the as-grown state and after being held in air at 650 °C over 2-h intervals up to 62 h. Figure 1d compares the evolution of $\mathrm{ASR_p}$ values over time for planar LSCF as well as LSCF-SDC and LSCF-HEO VAN films, with values normalized to the value of as-grown samples. Planar LSCF films exhibit an approximately linear increase in $\mathrm{ASR_p}$ over time, corresponding to a 238% increase after 62 h. The LSCF-SDC on the contrary is characterized by a 115% increase over the same time period, representing an approximate halving of the degradation rate. A similar degradation profile is observed for LSCF-HEO films, which are subject to a 98% $\mathrm{ASR_p}$ increase. A full understanding of the degradation mechanisms of the nanocomposite films is beyond the scope of the present work; however, one may consider that the reduced degradation rate is symptomatic of the reduced LSCF content. An alternative explanation is the presence of intermixing within the nanocomposite structure, as shown previously to yield enhanced stability in LSM-SDC nanocomposite films, where substitution of Ce into the LSM lattice is shown to mitigate Sr segregation.[10] Among the candidate materials studied, LSCF-SDC exhibited the lowest ASR at all temperatures, together with

Table 1. Summary of cathode materials under study.

Cathode composition	Abbreviation	Thickness (nm)	Area specific resistance at 600 °C	Activation energy (eV)
Au paste	Au	20 000	1451	1.05
$(La_{0.6}Sr_{0.4})_{0.95}Co_{0.2}Fe_{0.8}O_3$-MgO (MgO selectively etched)	LSCF-MgO	200	1135	1.31
Ag- $Gd_{0.20}(CeO_2)_{0.80}$	Ag-CGO	200	110[a)]	1.64
$(Ce_{0.2}La_{0.2}Sm_{0.2}Pr_{0.2}Y_{0.2})O_2$	HEO	200	7.83	1.74
$(La_{0.6}Sr_{0.4})_{0.95}Co_{0.2}Fe_{0.8}O_3$	LSCF	200	2.17	1.38
$(La_{0.60}Sr_{0.40})_{0.95}Co_{0.20}Fe_{0.80}O_3$ $(Ce_{0.2}La_{0.2}Sm_{0.2}Pr_{0.2}Y_{0.2})O_2$	LSCF-HEO	200	1.74	1.39
$(La_{0.60}Sr_{0.40})_{0.95}Co_{0.20}Fe_{0.80}O_3$-$(Sm_2O_3)_{0.20}(CeO_2)_{0.80}$	LSCF-SDC	200	1.28	1.40
$Sm_{0.2}Ce_{0.8}O_{1.9}$-$La_{0.8}Sr_{0.2}MnO_{3-d}$ + $(La_{0.6}Sr_{0.4})_{0.97}Co_{0.2}Fe_{0.8}O_3$	LSM-SDC + LSCF	18 000	0.47	1.23

[a)]Value based on linear extrapolation of experimental data measured up to 500 °C.

enhanced thermal stability compared with planar LSCF, and was therefore selected to be integrated into commercial Ni–YSZ anode supported half cells.

The complete device structure is shown by cross-sectional SEM in **Figure 2a**. This highlights the exceptionally low use of critical raw materials in the active cathode, which now accounts for approximately 0.0003% of the device mass (based on 200-nm-thick LSCF with a theoretical density of ~6.1 g cm^{-3} and a total device mass of 0.45 g).[27] Figure 2b presents high-resolution TEM of the LSCF-SDC nanocomposite structure, which is most clearly revealed by the contrast variations in Figure 2c when compared to the single-phase SDC buffer layer. EDX images (Figure 2d) reveal clean interfaces between the substrate, SDC buffer layer, and LSCF-SDC nanocomposite cathode layer, though are not able to clearly resolve the nanocomposite structure. We also note here some diffusion of the La, Sr, Co, and Fe through the SDC buffer layer; as mass transport contributions through the thin-film layers are negligible in the impedance of the full cell, this diffusion is not detrimental to device performance.

The performance of the complete Ni–YSZ/YSZ/LSCF-SDC fuel cell is characterized by current density-voltage and current density-power density plots (**Figure 3a**) at temperatures ranging from 600 °C to 750 °C. A successful gas-tight seal between the hydrogen and air chambers is first confirmed by an open circuit voltage (OCV) of 1.16 V. A maximum power density of 0.47 W cm^{-2} was achieved at 750 °C. Impedance spectra measured at open circuit voltage and under polarization at 0.5 A cm^{-2} are shown in Figure S5, Supporting Information. The data of the complete cells are modeled according to the fitting parameters shown in Table S1, Supporting Information with an equivalent circuit comprising three ZARC elements. As expected, the impedance under polarization is significantly reduced. Here we observe a low frequency arc with a capacitance of 1.67×10^{-1} F cm^{-2} and resistance of 0.13 Ωcm^2; these values are highly consistent with the 1.19×10^{-1} F cm^{-2} and 0.12 Ωcm^2 reported by Machado et al. and are therefore attributed to intrinsic impedances of the anode supported half cells, in particular to mass diffusion mechanisms in the Ni–YSZ anode.[17] The cathodic impedance attributed to the oxygen reduction reaction is described by an impedance arc with a capacitance of 1.96×10^{-3} F cm^{-2} and resistance of 0.53 Ωcm^2. This feature accounts for ~64% of the total cell impedance.

We next demonstrate the enhanced power output which can be achieved by cell operation in pure O_2 compared with synthetic air at the cathode. Figure S6, Supporting Information shows *I–V* and I–P plots for cells measured at 700 °C with different cathodic

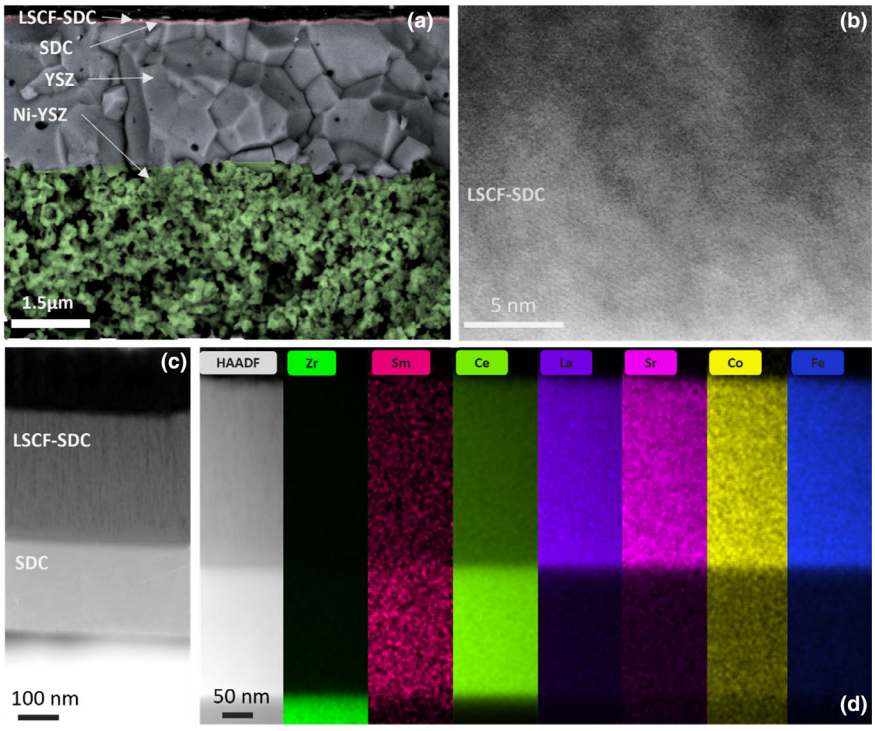

Figure 2. a) Cross-sectional SEM of commercial anode supported half cell with SDC buffer layer and LSCF-SDC nanocomposite cathode deposited by PLD; b) high-resolution TEM of LSCF-SDC nanocomposite structure; c) HAADF image showing SDC buffer layer and LSCF-SDC nanocomposite cathode; d) EDX mapping of SDC buffer layer and LSCF-SDC nanocomposite film.

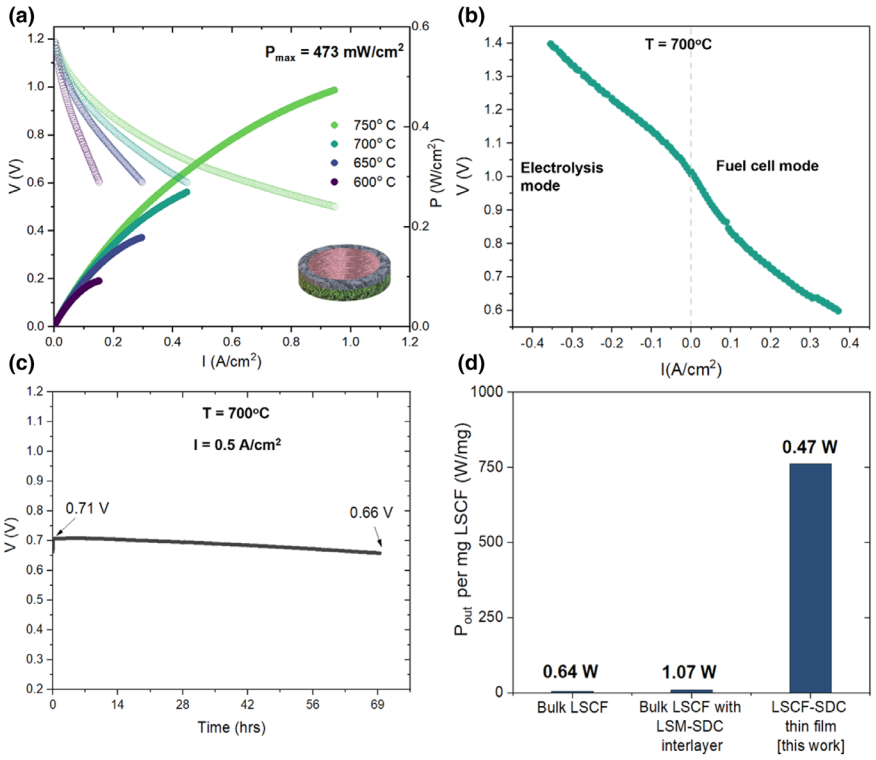

Figure 3. a) *I–V* and *I–P* curves for commercial anode supported half cell with LSCF-SDC thin-film cathode; b) *I–V* curves demonstrating device operation in fuel cell and electrolysis mode; c) stability test of the anode supported cell with thin-film cathode showing voltage drop over 72 h of operation at 0.5 A cm^{-2}; d) power output achieved presented per milligram of LSCF as compared with standard cells reliant on bulk LSCF.

atmospheres. A clear enhancement is revealed in the case of operation under pure oxygen, with a maximum power output of 0.4 W cm^{-2} compared with 0.26 W cm^{-2} under synthetic air.

We also explore the reversibility of the cell through operation under electrolysis conditions by applying a H_2/H_2O fuel mixed in a 1:1 ratio at 700 °C. Figure 3b shows *I–V* curves for the Ni–-YSZ/YSZ/LSCF-SDC cell in both fuel cell (SOFC) and electrolysis (SOEC) operation modes from which we observe a current density of 0.4 A cm^{-2} at 1.4 V. Comparable cells based on bulk Ni–YSZ/YSZ/$La_{0.8}Sr_{0.2}Co_{0.8}Ni_{0.2}$-GDC structures have previously achieved values of 0.75 A cm^{-2} at 1.4 V.[28] Therefore, although below state-of-the-art SOEC performance, the present work nevertheless highlights the promising applicability of VAN thin films for electrolysis operation and the development of reversible solid oxide cell devices with reduced CRM content.

Long-term stability characteristics of the cell are next considered by Figure 3c, which shows the evolution of the operating potential with the cell operating at 750 °C at an output current of 0.5 A cm^{-2} over 72 h. Nyquist plots for the full cell structure before and after degradation are given in Figure S7, Supporting Information and reveal a degradation profile consistent with that of the symmetric cells shown in Figure 1d, with a modest decrease in operating potential concomitant with a gradual increase in electrode impedance as observed previously. This result once again highlights the promising stability characteristics of nanocomposite thin films, though future work should be dedicated to further optimizing long-term stability, for instance through the design of protective coating layers.

Finally, it is instructive to consider the efficiency of material usage by comparing the peak power density of the cell (0.47 W cm^{-2}) with the value of 0.64 W cm^{-2}, which can be achieved using the same anode support structure with a bulk 18-μm-thick LSCF cathode.[17] This is summarized by Figure 3d, in which the power outputs of cells with and without bulk LSCF cathodes are compared, while taking into account the mass contribution of LSCF. In this context, cells with only the LSCF-SDC thin-film cathode deliver ~760 W mg^{-1} of LSCF, as compared to ~5.7 W mg^{-1} for conventional bulk LSCF. Thus, the novel nanocomposite LSCF-SDC thin-film cathode can be seen to offer a drastic enhancement in the efficiency of the cathodic performance, when considering the effective utilization of the active cathode material.

3. Conclusion

In this work, we have presented a performance comparison of six candidate thin-film cathode materials for integration directly into commercial anode supported solid oxide fuel cells. By comparing the

Table 2. Summary of pulsed laser deposition conditions for each material under study.

Material	*T* (°C)	Repetition rate (Hz)	Atmosphere	Gas flow rate (sccm)	Fluence (J cm^{-2})
$(Sm_2O_3)_{0.20}(CeO_2)_{0.80}$	750	10	7×10^{-3} mBar O_2	0.7	1.0
$(La_{0.6}Sr_{0.4})_{0.95}Co_{0.2}Fe_{0.8}O_3$	600	3	0.4 mBar O_2	6	3.2
$(La_{0.60}Sr_{0.40})_{0.95}Co_{0.20}Fe_{0.80}O_3$-$(Sm_2O_3)_{0.20}(CeO_2)_{0.80}$	600	3	0.4 mBar O_2	6	3.2
$(La_{0.6}Sr_{0.4})_{0.95}Co_{0.2}Fe_{0.8}O_3$-MgO	600	3	0.4 mBar O_2	6	0.8
Ag- $Gd_{0.10}(CeO_2)_{0.90}$	280	10	6×10^{-6} mBar O_2	0	0.8
$(Ce_{0.2}La_{0.2}Sm_{0.2}Pr_{0.2}Y_{0.2})O_2$	600	3	0.4 mBar O_2	6	1.6
$(La_{0.60}Sr_{0.40})_{0.95}Co_{0.20}Fe_{0.80}O_3$ $(Ce_{0.2}La_{0.2}Sm_{0.2}Pr_{0.2}Y_{0.2})O_2$	600	3	0.4 mBar O_2	6	3.2

electrochemical performance of each, established by impedance spectroscopy measurements, we show that nanocomposite thin films such as LSCF-SDC exhibit reduced ASR values, as low as $0.44\,\Omega cm^2$ at 650 °C, and enhance long-term stability compared with planar LSCF thin films. We then demonstrate the successful deposition of these LSCF-SDC nanocomposite thin films onto commercial anode supported half cells. Complete cells with only the 200-nm-thick thin-film nanocomposite cathode exhibit peak power density of $0.47\,W\,cm^{-2}$ at 750 °C and are thus competitive with equivalent cells based on conventional bulk LSCF cathodes. Moreover, the cells exhibit reversible functionality, with a current density of $0.4\,A\,cm^{-2}$ at 1.4 V achieved in electrolysis operation mode at 700 °C. Such competitive performance is achieved, despite a ∼99.5% reduction in LSCF content. This work therefore marks a promising route to the sustainable development of SOFC technology through a drastic reduction in critical raw material dependence, achieved through vertically aligned nanocomposite thin films which can be directly integrated into commercial cells through a single-step deposition process.

4. Experimental Section

$(La_{0.60}Sr_{0.40})_{0.95}Co_{0.20}Fe_{0.80}O_3$ (LSCF) powder was supplied by Nexceris, LLC, and $(Sm_2O_3)_{0.20}(CeO_2)_{0.80}$ (SDC) and MgO powders were supplied by Alfa Aesar. $Ce_{0.9}Gd_{0.1}O_{2-d}$ (GDC) powder and Ag metal were supplied by Praxair and Merck, respectively. The HEO (Ce,La,Pr,Sm,Y)O_2 was synthesized by the Pechini process, a variation of Sol–Gel. A precursor solution was made by dissolving stoichiometric amounts of $Ce(NO_3)_3{\cdot}6H_2O$ (Alfa Aesar – 99.95%), $La(NO_3)_3{\cdot}6H_2O$ (Thermo Scientific – 99.9%), $Pr(NO_3)_3{\cdot}6H_2O$ (Alfa Aesar – 99.99%), $Sm(NO_3)_3{\cdot}6H_2O$ (Thermo Scientific – 99.9%), and $Y(NO_3)_3{\cdot}6H_2O$ (Sigma-Aldrich – 99.8%) in water. Citric acid (Sigma-Aldrich – 99.5%) (a chelating agent) and ethylene glycol (Alfa Aesar – 99%) (a polymerizing agent) were added to the precursor solution. The precursor solution was then aged on a hot plate at 150 °C for 1 h to form a polymer chain around the metal cations. The resultant polymer gel was then completely dried on the hot plate at 300 °C. The dried powder was then calcined at 750 °C for 6 h resulting in HEO nanoparticles. Ceramic targets were prepared for pulsed laser deposition (PLD) using an agate pestle and mortar to grind ∼3 g powder for 30 min. For nanocomposite films, powders of two materials were mixed in a 50:50 wt.% ratio (70:30 for Ag-CGO). Ground powders of LSCF, LSCF-SDC, LSCF-MgO, and LSCF-HEO were pelletized with a 10 ton isostatic press before sintering at 1300 °C for 4 h, with a heating/cooling rate of $5\,°C\,min^{-1}$. Ag-CGO targets were pressed isostatic the at 350 MPa and sintered at 900 °C for 2 h. HEO target (diameter 25.4 mm) was pelletized with a10 ton uniaxial press and sintered at 1000 °C for 12 h.

Films were grown on (001) oriented $(Y_2O_3)_{0.095}(ZrO_2)_{0.905}$ (CrysTec GmbH), polycrystalline $(Y_2O_3)_{0.08}(ZrO_2)_{0.92}$ button substrates (KERAFOL), and anode supported half cells (SolydEra SpA). PLD was performed with a 248 nm KrF laser (Lambda Physik, Inc) with ceramic targets held 45 mm from the substrate. Before all depositions, the PLD chamber was evacuated to at least 7×10^{-7} mbar and then heated to the desired temperature. Films were grown according to the conditions described in **Table 2** below. Following deposition, samples were cooled to room temperature at $10\,°C\,min^{-1}$ in the same atmosphere in which they were grown. Polycrystalline YSZ substrates were first coated with a 200-nm-thick SDC buffer layer before deposition of the active cathode layer to mitigate the formation of secondary phases.

A Panalytical Empyrean high-resolution X-ray diffractometer with Cu-Kα radiation (λ = 1.5405 Å) was used for X-ray diffraction measurements.

A ProboStat™ (NorECS) system, placed inside a high temperature tube furnace, was used for fuel cell characterizations with dry H_2 and synthetic air supplied to the fuel and oxygen electrodes, respectively, at rates of 150 and $300\,Nml\,min^{-1}\,cm^{-2}$. A gas-tight seal between the fuel and oxygen electrodes was achieved by application of Ceramabond™ paste (Aremco). *I–V* measurements were conducted with a M9700 electronic load from Maynuo Electronic Co. Ltd. and PARSTAT® 2273 potentiostat, and a Novocontrol impedance spectrometer was used for EIS measurements over a frequency range 10^6–0.1 Hz and voltage amplitude of 50 mV. A porous Au paste current collector was applied to the oxygen electrodes for full cell and symmetric cell measurements. A Ni-paste current collector was likewise applied to the fuel electrode for full cell measurements.

High angle annular dark field STEM measurements were performed on a probe aberration corrected Thermo Fisher Scientific Spectra 300 with a 300 keV, 100 pA electron beam, and a dwell time of 10 µs. Convergence and collection angles were to 24 mrad and 60–200 mrad, respectively. Energy dispersive x-ray signal were recorded of 4 Super-X detectors, with multiframe acquisition. Samples were prepared using FEI Helios Nanolab SEM/FIB using standard FIB lamella techniques. Image analysis was carried out using Velox software.

Acknowledgements

M.P.W. and K.K. contributed equally to this work and are designated as co-first authors. M.P.W., K.K., M.B., O.C., J.P.O., A.T., and J.L.M.-D. acknowledge the European Union's Horizon 2020 research and innovation program (grant number 101017709) (EPISTORE). J.L.M.-D. also acknowledges support from the Royal Academy of Engineering Chair in Emerging technologies (grant number CIET1819_24), and the EPSRC Centre of Advanced Materials for Integrated Energy Systems (CAM-IES) (grant number EP/P007767/1) and the EU-H2020-ERC-ADG EROS (grant number 882929). M.V.K. and M.B. are grateful for the support provided by Deutsche Forschungsgemeinschaft (Project no. 424789449, grant no. HA1344-45-1). O.C. also acknowledges support from the European Union's Horizon 2020 research and innovation program under the Marie Sklodowska-Curie grant agreement no. 836503. We acknowledge use of the Thermo Fisher Spectra 300 TEM at the Wolfson Electron Microscopy Suite at the University of Cambridge funded by EPSRC under grant EP/R008779/1.

Conflict of Interest

The authors declare no conflict of interest.

Supporting Information

Supporting Information is available from the Wiley Online Library or from the author.

Keywords

solid oxide fuel cells, thin films, vertically aligned nanocomposites

Received: August 22, 2024
Revised: January 10, 2025
Published online: February 2, 2025

[1] S. He, Y. Zou, K. Chen, S. P. Jiang, *Interdiscip. Mater.* **2023**, *2*, 111.
[2] O. Yamamoto, *Electrochim. Acta* **2000**, *45*, 2423.
[3] Y. Wang, A. Banerjee, L. Wehrle, Y. Shi, N. Brandon, O. Deutschmann, *Energy. Conver. Manage.* **2019**, *196*, 484.
[4] A. Bieberle-Hütter, D. Beckel, A. Infortuna, U. P. Muecke, J. L. M. Rupp, L. J. Gauckler, S. Rey-Mermet, P. Muralt, N. R. Bieri, N. Hotz, M. J. Stutz, D. Poulikakos, P. Heeb, P. Müller, A. Bernard, R. Gmür, T. Hocker, *J. Power Sources* **2008**, *177*, 123.
[5] J. C. Ruiz-Morales, D. Marrero-López, J. Canales-Vázquez, J. T. S. Irvine, *RSC Adv.* **2011**, *1*, 1403.
[6] S. Biswas, D. S. Dhawale, T. Hosseini, G. Kaur, S. Giddey, N. Haque, *ACS Sustain. Chem. Eng.* **2024**, *12*, 6037.

[7] W. Ma, J. J. Kim, N. Tsvetkov, T. Daio, Y. Kuru, Z. Cai, Y. Chen, K. Sasaki, H. L. Tuller, B. Yildiz, *Pharm. Biol.* **2025**, *63*, 156.
[8] M. Acosta, F. Baiutti, A. Tarancón, J. L. MacManus-Driscoll, *Adv. Mater. Interfaces* **2019**, *6*, 1900462.
[9] M. Acosta, F. Baiutti, X. Wang, A. Cavallaro, J. Wu, W. Li, S. C. Parker, A. Aguadero, H. Wang, A. Tarancón, J. L. MacManus-Driscoll, *J. Power Sources* **2022**, *523*, 230983.
[10] F. Baiutti, F. Chiabrera, M. Acosta, D. Diercks, D. Parfitt, J. Santiso, X. Wang, A. Cavallaro, A. Morata, H. Wang, A. Chroneos, J. MacManus-Driscoll, A. Tarancon, *Nat. Commun.* **2021**, *12*, 2660.
[11] M. P. Wells, A. J. Lovett, T. Chalklen, F. Baiutti, A. Tarancón, X. Wang, J. Ding, H. Wang, S. Kar-Narayan, M. Acosta, J. L. Macmanus-Driscoll, *ACS Appl. Mater. Interfaces* **2021**, *13*, 4117.
[12] F. Hess, B. Yildiz, *Phys. Rev. Mater.* **2020**, *4*, 015801.
[13] N. Tsvetkov, Q. Lu, L. Sun, E. J. Crumlin, B. Yildiz, *Nat. Mater.* **2016**, *15*, 1010.
[14] Y. Shi, N. Ni, Q. Ding, X. Zhao, *Angew. Chem. Int. Ed.* **2025**, *10*, e202503898.
[15] C. W. Kwon, J. W. Son, J. H. Lee, H. M. Kim, H. W. Lee, K. B. Kim, *Adv. Funct. Mater.* **2011**, *21*, 1154.
[16] M. P. Wells, A. J. Lovett, Y. Zhang, Z. Shang, K. Kreka, B. Bakhit, H. Wang, A. Tarancón, J. L. MacManus-Driscoll, *Nano Energy* **2024**, *119*, 109049.
[17] M. Machado, F. Baiutti, L. Bernadet, A. Morata, M. Nuñez, J. P. Ouweltjes, F. C. Fonseca, M. Torrell, A. Tarancón, *Int. J. Cardiol.* **2025**, *10*, 133088.
[18] F. Buzi, K. Kreka, J. Santiso, L. Rapenne, Z. Sha, J. Douglas, F. Chiabrera, A. Morata, M. Burriel, S. Skinner, L. Bernadet, F. Baiutti, A. Tarancón, *ACS Appl. Mater. Interfaces* **2024**, *16*, 43462.
[19] D. Beckel, U. P. Muecke, T. Gyger, G. Florey, A. Infortuna, L. J. Gauckler, *Solid State Ion.* **2007**, *178*, 407.
[20] F. Zhou, Y. Liu, X. Zhao, W. Tang, S. Yang, S. Zhong, M. Wei, *World J. Clin. Oncol.* **2025**, *16*, 99635.
[21] O. Celikbilek, M. Wells, J. L. Driscoll, S. Skinner, *ECS Meet. Abstr.* **2021**, *MA2021-02*, 1377.
[22] J. Huang, J. L. MacManus-Driscoll, H. Wang, *J. Mater. Res.* **2017**, *32*, 4054.
[23] K. Develos-Bagarinao, T. Ishiyama, H. Kishimoto, H. Shimada, K. Yamaji, *Nat. Commun.* **2021**, *12*, 3979.
[24] V. Dusastre, J. A. Kilner, *Solid State Ion.* **1999**, *126*, 163.
[25] M. Acosta, F. Baiutti, X. Wang, A. Cavallaro, J. Wu, W. Li, S. C. Paker, A. Aguadero, H. Wang, A. Tarancón, J. L. MacManus-Driscoll, unpublished.
[26] H. Zhao, W. Li, H. Wang, J. Zhou, X. Sun, E. Wang, L. Zhao, B. Dong, S. Wang, *Appl. Surf. Sci.* **2022**, *572*, 151382.
[27] S. P. Jiang, *Int. J. Hydrogen Energy* **2019**, *44*, 7448.
[28] Y. Tan, N. Duan, A. Wang, D. Yan, B. Chi, N. Wang, J. Pu, J. Li, *J. Power Sources* **2016**, *305*, 168.